

RESEARCH

Open Access



# Influence of Pore Structure Characteristics on the Mechanical and Durability Behavior of Pervious Concrete Material Based on Image Analysis

Ruyan Liu<sup>1</sup>, Yin Chi<sup>1</sup>, Shengyun Chen<sup>2</sup>, Qinghui Jiang<sup>1\*</sup> , Xiaoyu Meng<sup>1</sup>, Kun Wu<sup>1</sup> and Shengjia Li<sup>1</sup>

## Abstract

Pervious concrete has been widely used in parking lots and other lightweight streets. Performances of pervious concrete are strongly dependent on its pore structure characteristics. This paper investigates the relationship among porosity, permeability, compressive strength, durability and the pore structure characteristics of pervious concrete. The influences of basalt fiber and fine aggregate on the pervious concrete are also discussed. Pervious concrete specimens with different pore structures were prepared by combining basalt aggregate with size of 5–10 mm and 10–15 mm at different proportion. The pore structure characteristics such as area porosity, pore sizes, and pore distribution of pervious concrete were obtained and analyzed using image analysis method. Experimental results showed that the pore structure characteristics of pervious concrete have effects on its mechanical and durability behaviors. Homogeneous pore distribution and large distances between pores increase the compressive strength and improve freeze–thaw durability of pervious concrete. Due to the difference in the internal pore structure of pervious concretes, specimens with similar volumetric porosities had different permeability coefficients. A series of numerical models were regenerated through a MATLAB code using pore structural parameters derived from the image analysis method, then the numerical models were fed to ANSYS for meshing and further simulation. The comparison of the simulation and experimental results showed close accuracy, which verified the applied simulation analysis method based on image analysis technology.

**Keywords:** pervious concrete, image analysis, pore structure, strength, permeability, durability, numerical simulation

## 1 Introduction

Pervious concrete is a kind of pervious material consisting of coarse aggregate, cement, water, little or no content of fine aggregate and admixtures. The porosity of pervious concrete is between 15 and 25% (Huang et al. 2010; Ibrahim et al. 2014). With high porosity and connected pore system, pervious concrete is of great help to accelerate storm runoff, recharge groundwater, absorb

the noise and insulate the thermal (Nguyen et al. 2014; Shen et al. 2012; Chen et al. 2013; Zhong and Wille 2015). These advantages of being environmentally friendly of pervious concrete have aroused a worldwide attention for researchers. Extensive researches have been studied on the mechanical, permeable and durable properties of this material. The properties of cement paste, aggregate and interfacial transition zone are three main aspects that affect the performance of pervious concrete (Huang et al. 2010; Chindapasirt et al. 2009; Luck et al. 2008; Jimma and Rangaraju 2014; Deo and Neithalath 2011; Keven et al. 2010). Although fundamental factors including the water-binder ratio, supplementary cementitious

\*Correspondence: jqh1972@whu.edu.cn

<sup>1</sup> School of Civil Engineering, Wuhan University, Wuhan 430072, Hubei, People's Republic of China

Full list of author information is available at the end of the article

Journal information: ISSN 1976-0485 / eISSN 2234-1315

materials, type and size of coarse aggregate, aggregate-binder ratio, sand ratio and micro study of the interfaces have been studied (Čosić et al. 2015; Tittarelli et al. 2014; Joshaghani et al. 2014; Carsana et al. 2013; Tittarelli et al. 2013; Yang and Jiang 2003; Neithalath 2007; Bonicelli et al. 2015; Haselbach et al. 2006), very few investigations are conducted with regards to the relationship between aggregate gradation and pore structure and the influence of them on the permeability and durability of pervious concrete. The pore structures are generally considered to include porosity, pore size, pore distribution and tortuosity of macro voids.

The influence of the coarse aggregate gradation on the properties of pervious concrete was studied in the (Xu et al. 2018; Yang et al. 2008; Mrakovčić et al. 2014; Chandrappa and Biligiri 2016). Results in (Yang et al. 2008) showed that the strength of pervious concrete increased with the increase of fine aggregate content, whereas decreased with the increase of the maximum size of coarse aggregate. The suitable volume content of 4.75–9.5 mm particle in coarse aggregate was around 20%, so the coarse aggregate had little interference with the secondary aggregate and the pervious concrete could have high strength and satisfied permeability. Deo and Neithalath (2011) studied the porosity and pore structure of pervious concrete with different size of aggregate. Wong et al. (2006) presented a technique to distinguish pores from a normal backscattered electron image of cement-based material. Pore size distribution was generally obtained from Mercury Intrusion Porosimetry (MIP) (Wu et al. 2013) or image analysis method (Akand et al. 2016) and then was taken as the basis for reconstruction of simulated models. Deo and Neithalath (2010) stated that the properties of pervious concrete were strongly dependent on its pore structure characteristics. In their study, several pervious concrete mixtures with different pore structure characteristics were proportioned and were subjected to compression tests. The pore structure characteristics were extracted using image analysis methods. The compressive response was found to be influenced by the pore size, pore distribution and pore spacing. Neithalath et al. (2010) investigated methods of characterizing the pore structure characteristics in pervious concrete material and predicted permeability based on these pore structure characteristics. It showed that maximization of water permeability behavior of pervious concretes was best achieved by increasing the pore connectivity. The study described a critical point where a small incremental gray value caused a sudden increase in porosity estimation, a condition was termed as overflow. In order to explore the relationship between pore structure and properties of pervious concrete, image analysis method was used and the pore structure characteristics

including pore size, spacing, and distribution were analyzed in present study.

Fibers can efficiently improve the mechanical properties and freeze–thaw durability (Hesami et al. 2014; Wu et al. 2016; Kevern et al. 2015; Rangelov et al. 2016). Fibers can also improve the internal structures of pervious concrete (Wu et al. 2013). However, there are few studies on the pore structure of fiber reinforced pervious concrete, some macroscopic behavior changes cannot be reasonably explained from microscopic level (Vipulanandan and Liu 2008). In this study, pervious concrete modified with fly ash, silica fume, basalt fiber and superplasticizer was prepared. Two sizes of basalt aggregate including 5–10 mm and 10–15 mm were selected as coarse aggregate and combined in different proportions. A total of 9 different pervious concrete mixtures with different pore structures were proportioned. The compressive strength, permeable performance and durability of the pervious concrete with these proportions were tested. Simultaneously, image analysis method was applied to study the pore structures such as area porosity, pore size, pore spacing, and pore distribution of pervious concrete. The relationships among pore structure characteristics and porosity, permeability, compressive strength, durability were studied. The influences of basalt fiber and fine aggregate on the performance of pervious concrete were also involved. Using the derived pore structure parameters through Image J, microstructure models were regenerated through a MATLAB code and were fed to ANSYS for meshing and further simulation, respectively. The simulated stress–strain plots of 2D specimens under compressive load were compared with the plots from the lab experiments, which was used to confirm the proposed simulation analysis method based on image analysis technology.

## 2 Experimental Program

### 2.1 Materials

The materials used in the present study included coarse aggregate, sand, cementitious materials, fiber and water. Ordinary Portland Cement P.O 52.5 according to GB 175-2007 (GB 2007), silica fume and fly ash were selected as cementitious materials.

Ordinary Portland Cement P.O 52.5 also meets the requirements of EN 197-1:2011 (NSAI 2011). The physical properties and chemical compositions of the cement are shown in Tables 1 and 2, respectively. The apparent density and specific surface area of silica fume are 2200 kg/m<sup>3</sup> and 24,000 m<sup>2</sup>/kg, respectively. The common ranges of chemical compositions of silica fume used in China are shown in Table 3. The fly ash used has a fineness of 6.7% and a loss on ignition of 1.6%. Chemical

**Table 1 Physical properties of cement.**

Initial setting time (min)	Final setting time (min)	Compressive strength (MPa)		Flexural strength (MPa)		specific surface area (m <sup>2</sup> /kg)	Consistency (Redwood method) (mm)
		7-day	28-day	7-day	28-day		
145	192	34.5	58.8	7.2	10.4	362	0.5

**Table 2 Chemical compositions of the cement.**

Composition	CaO	SiO <sub>2</sub>	Al <sub>2</sub> O <sub>3</sub>	Fe <sub>2</sub> O <sub>3</sub>	MgO	SO <sub>3</sub>	Loss on ignition
Mass fraction	61.16%	21.28%	5.93%	3.38%	1.64%	2.02%	2.26%

**Table 3 Common ranges of chemical compositions of silica fume used in China.**

Composition	SiO <sub>2</sub>	Al <sub>2</sub> O <sub>3</sub>	Fe <sub>2</sub> O <sub>3</sub>	CaO	MgO	Na <sub>2</sub> O
Mass fraction	80–92%	0.8–1.2%	0.6–1.2%	0.2–0.4%	0.6–0.8%	1.1–1.5%

**Table 4 Chemical compositions of fly ash from 31 representative thermal power stations in China.**

Composition	SiO <sub>2</sub>	Al <sub>2</sub> O <sub>3</sub>	Fe <sub>2</sub> O <sub>3</sub>	CaO	MgO	K <sub>2</sub> O	Na <sub>2</sub> O	SO <sub>3</sub>	Loss on ignition
Mass fraction	33.9–59.7%	16.5–35.4%	1.5–19.7%	0.8–10.4%	0.7–1.9%	0.6–2.9%	0.2–1.1%	0.0–1.1%	1.2–23.6%
Mean value	50.6%	27.1%	7.1%	2.8%	1.2%	1.3%	0.5%	0.3%	8.2%

compositions of fly ash from 31 representative thermal power stations in China are shown in Table 4.

Two different single-sized basalt gravels including 5–10 mm and 10–15 mm were used as coarse aggregate. The apparent density of basalt gravel was 3159 kg/m<sup>3</sup>. In order to study the influence of fine aggregate on pore structure of pervious concrete, natural river sand was used as fine aggregate and mainly ranged from 0.5 to 2.5 mm in size.

A basalt fiber was incorporated to investigate its influence on the performance of pervious concrete. The diameter and the length of the basalt fiber were 15  $\mu$ m and 20 mm, respectively. The tensile strength of the basalt fiber was 4100–4840 MPa.

In addition, a superplasticizer was used to improve the workability of fresh concrete. The superplasticizer was a type of high range polycarboxylate water reducer. The solid content and water reducing ratio of the superplasticizer were 20% and 25%, respectively.

## 2.2 Mix Proportion Design

The method for mix proportion design of pervious concrete in this study was on the basis of ACI 522R-10 (ACI 2010). The water-binder ratio was 0.22 of all the proportions in this experiment. Fly ash (FA) and silica fume

(SF) were incorporated by replacing 10% and 7.5% of the cement by weight, respectively. Fine aggregate to total aggregate ratio by mass was set as 7%. Besides, basalt fiber was added in a volume content of 0.2%. The target porosity in this study was selected as 15%. The details of mix proportion are shown in Table 5.

## 2.3 Specimen Preparation

The original materials were mixed in forced action concrete mixer. Firstly, all coarse aggregate and half of water were mixed for 1 min. Then, the cement, fly ash, silica fume, basalt fiber and other half of the water were added to the mixer and mixed for another 1 min. Lastly, the superplasticizer was added into the aforementioned pervious concrete mixtures and all materials were mixed altogether for about 50 s, which depended on workability of the fresh concrete mixtures.

A total of 243 specimens were prepared consisting of 27 cube specimens with size of 150 mm  $\times$  150 mm  $\times$  150 mm for compression tests, 135 cube specimens with size of 100 mm  $\times$  100 mm  $\times$  100 mm for freeze-thaw durability tests, 27 cube specimens with size of 150 mm  $\times$  150 mm  $\times$  150 mm for volumetric porosity tests, 27 cylinder specimens with size of 100 mm  $\times$  50 mm for permeability tests and 27 cylinder

**Table 5 Mix proportion of the specimens.**

Mix proportion	No.	5-CA (kg/m <sup>3</sup> )	10-CA (kg/m <sup>3</sup> )	Sand (kg/m <sup>3</sup> )	Cement (kg/m <sup>3</sup> )	FA (kg/m <sup>3</sup> )	SF (kg/m <sup>3</sup> )	Fiber (kg/m <sup>3</sup> )	Water (kg/m <sup>3</sup> )	SP (kg/m <sup>3</sup> )
100% 5-CA + 0% 10-CA	P1	1738	0	0	471	47	35	0	122	8
75% 5-CA + 25% 10-CA	P2	1303	434	0	471	47	35	0	122	8
50% 5-CA + 50% 10-CA	P3	869	869	0	471	47	35	0	122	8
25% 5-CA + 75% 10-CA	P4	434	1303	0	471	47	35	0	122	8
0% 5-CA + 100% 10-CA	P5	0	1738	0	471	47	35	0	122	8
93% 10-CA + 7% sand	PS1	0	1616	122	471	47	35	0	122	8
46.5% 5-CA + 46.5% 10-CA + 7% sand	PS2	808	808	122	471	47	35	0	122	8
93% 5-CA + 7% sand	PS3	1616	0	122	471	47	35	0	122	8
93% 5-CA + 7% sand + 0.2% fiber	PSF1	1616	0	122	471	47	35	5.4	122	8

In the symbol string “a% b-CA”, a represents volume ratio, b represents the size of coarse aggregate which is b ~ (b + 5) mm, CA represents coarse aggregate, SP represents superplasticizer.

specimens with size of 100 mm × 50 mm for image analysis. The appearances of all specimens are shown in Fig. 1. Concrete mixtures were cast into molds and compacted as much as possible with a small steel shovel before the cementitious slurry solidified. All the specimens were placed in molds for 24 h for shaping. After demolding, all specimens were moist-cured in a standard curing room at 20 °C constantly and 95% relative humidity for 28 days.

**2.4 Test Procedure**

**2.4.1 Volumetric Porosity Test**

The volumetric porosity of pervious concrete specimens was determined in accordance with ASTM C1754/C1754-12 (ASTM 2012). Specimens were oven-dried at 60 °C for 24 h and were weighed firstly. Subsequently, the specimens were saturated after being immersed in water for 30 min and were then weighed again. Based on the weight of the oven-dried specimens and the water-saturated specimens, the volumetric porosity of specimens of pervious concrete was calculated using Eq. (1).

$$P = \left( 1 - \frac{m_1 - m_2}{V \cdot \rho_w} \right) \times 100\% \tag{1}$$

where  $P$  is the volumetric porosity,  $m_1$  (kg) is the mass of the oven-dried specimen,  $m_2$  (kg) is the mass of the water saturated specimen,  $\rho_w$  (kg/m<sup>3</sup>) is the water density, and  $V$  (m<sup>3</sup>) is the volume of the specimen.

**2.4.2 Permeability Test**

According to ASTM D5856-15 (ASTM 2015), the permeability coefficient of pervious concrete was measured under the constant water head using the permeameter as shown in Fig. 2. In order to ensure that the water only permeated from the upper surface to the lower surface of specimens, a type of industrial butter was smeared around sides of specimens and perimeter of the upper

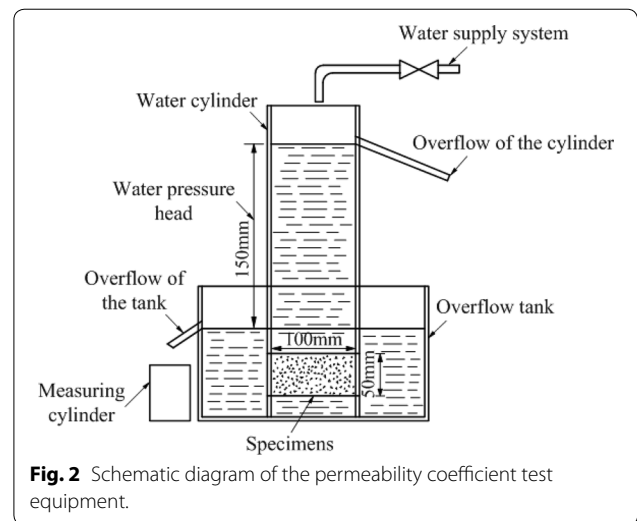


**Fig. 2** Schematic diagram of the permeability coefficient test equipment.

surface of specimens, as displayed in Fig. 3. Moreover, it was required that specimens should be vacuum saturated before permeability test.

After the specimen was connected and sealed well with water storage cylinder, it was placed together into overflow tank. Then inlet water valve was opened and airless water was injected into container. When the water was out from the overflow, the water level of water storage cylinder was kept constant (150 mm) by adjusting the inflow of water. After outflow of water from the water storage cylinder and the overflow tank were stable, the water was held with a measuring cylinder and its volume in 5 min was measured. The final outflow of water was the average value of the three measurements. Finally, water head between the water storage cylinder and the overflow tank was measured with a steel ruler. The permeability coefficient of specimens was calculated by Eq. (2).

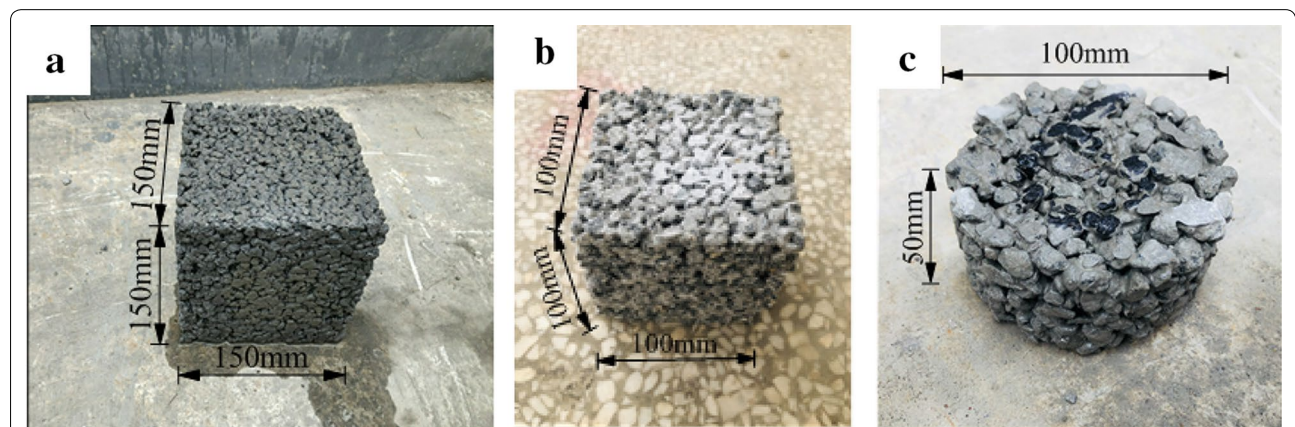


**Fig. 1** Appearance of **a** cube specimen with sides 150 mm, **b** cube specimen with sides 100 mm, and **c** cylinder specimen.

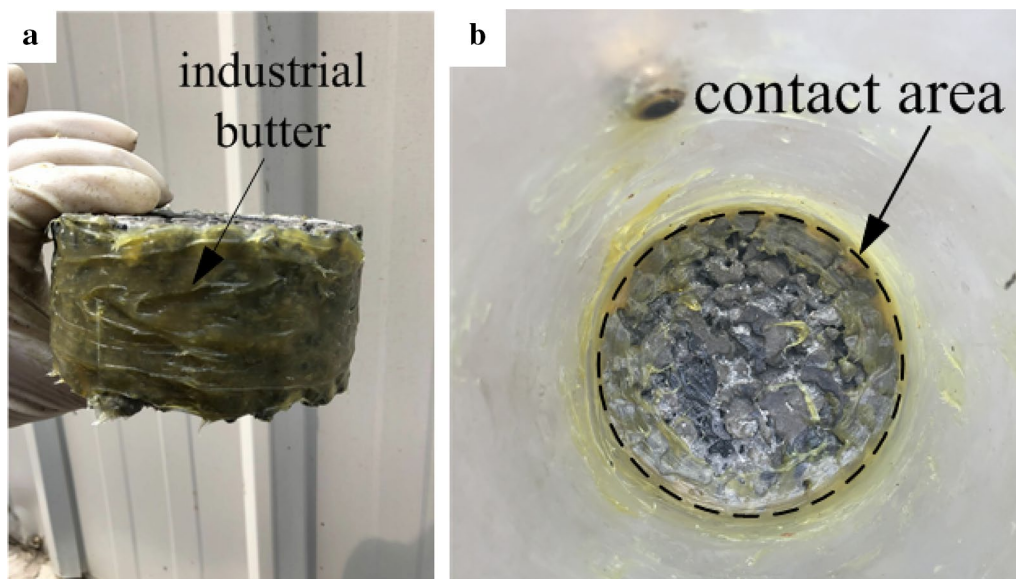


**Fig. 3** Specimens smeared with industrial butter on the **a** side of specimens, and **b** top perimeter of specimens.

$$k = QL/Aht \quad (2)$$

Where  $k$  is permeability coefficient (mm/s),  $Q$  is the quantity of water flow between  $t$  time period (mm<sup>3</sup>),  $L$  is the length of the specimen (mm),  $A$  is the top cross sectional area of the specimen (mm<sup>2</sup>),  $h$  is the water head (mm),  $t$  is the time measured (s).

#### 2.4.3 Compression Test

Uniaxial compression tests were conducted on a servo-hydraulic rock/concrete material test system RMT-301, using standard 150 mm × 150 mm × 150 mm cube specimens. The specimen was tested using a Hydraulic Servo System with displacement-control loading. The loading rate was set as 0.02 mm/s to achieve a quasi-static loading. The compressive process was not terminated until a large stress drop occurred in the specimen. Three specimens were performed for each mix proportion and the average value was selected as the representative strength of that mix proportion.

#### 2.4.4 Durability Test

Cube specimens of 100 mm × 100 mm × 100 mm were subjected to freeze–thaw durability tests using type DWR-4 Automatic Low Temperature Freeze–thaw Testing Machine, in accordance with GB/T 50082-2009 standard of slow freeze–thaw procedure (GB/T 2009). The freeze–thaw cycles in the present study were carried out under the condition of air-freezing and water-thawing. The freeze–thaw procedure in GB/T 50082-2009 referred to in this study corresponds to Procedure B

(rapid freezing in air and thawing in water) in ASTM C666/C666M-03 (ASTM 2015). The specimen size, freeze–thaw process and related regulations in the two standards are the same. The difference is that the two standards have different indexes to evaluate the experimental results. The standard of GB/T 50082-2009 uses loss rate of compressive strength and the loss rate of mass of specimens to measure the frost resistance of concrete. In ASTM C666/C666M-03, the evaluation indexes of freeze–thaw procedures are relative dynamic modulus of elasticity, endurance factors and the percentages of length changes of the specimens. Both indexes in the two standards can be used to determine the effects of experimental variables on the freeze–thaw cycle performance of concrete. Considering our experimental conditions, the freeze–thaw durability test method was referred to GB/T 50082-2009 in the study.

Five sets for each mix proportion were prepared in the present slow freeze–thaw tests. One set was used to determine 28-day compressive strength, two sets were prepared for the freeze–thaw tests and another two sets were taken as control groups. Specimens of the control groups were maintained under the curing conditions until the completion of the freeze–thaw cycles, then these specimens were subjected to uniaxial compression tests simultaneously with the specimens of the freeze–thaw groups. During the freeze–thaw process, both the temperature of freezing in the chamber and the temperature of injected water were –18 to –20 °C. Water level in the freeze–thaw chamber was above the top of the specimens for 20 mm. The time of each freeze–thaw cycle

was 4 h. Appearance and mass of the specimens were examined every 25 freeze–thaw cycles. The freeze–thaw process was not terminated until the number of cycles reached specified number of cycles, until the loss rate of compressive strength of specimens reached to 25% or until the loss rate of mass of specimens reached to 5%, whichever occurred first. The loss rate of compressive strength was calculated by Eq. (3).

$$\Delta f_c = \frac{f_{c0} - f_{cn}}{f_{c0}} \times 100\% \quad (3)$$

where  $\Delta f_c$  is the loss rate of the compressive strength (%), after N freezing and thawing cycles, accurate to 0.01;  $f_{c0}$  is the compressive strength of the specimens of the control group (MPa);  $f_{cn}$  is the compressive strength of the freeze–thaw specimens (MPa), after N freezing and thawing cycles.

The loss rate of mass was calculated by Eq. (4).

$$\Delta W_n = \frac{W_0 - W_n}{W_0} \times 100\% \quad (4)$$

where  $\Delta W_n$  is the loss rate of mass (%), after N freezing and thawing cycles, accurate to 0.01;  $W_0$  is the mass of the freeze–thaw specimens at 0 freeze–thaw cycles (kg);  $W_n$  is the mass of the freeze–thaw specimens (kg), after N freezing and thawing cycles.

#### 2.4.5 Image Analysis Processing and Pore Structure Characteristics Acquiring

Image analysis method was conducted on 2D images of pervious concrete specimens to obtain pore structure characteristics. For each mix proportion, three cylinder specimens of 100 mm in diameter and 50 mm in length were used. Slices of 10 mm thick were removed from top and bottom of each specimen, and the remaining 30 mm thick slice of each specimen was used for image analysis. Therefore, three sections and six images were prepared for each mix proportion. The cut cross sections were photographed and were processed using an image processing and analysis software Image J. The original photographs were converted into binary images by a thresholding operation. The binary images were further processed to remove noise. Finally, 400 pixel  $\times$  400 pixel square images were obtained and were used to extract the pore structure characteristics. The schematic of the image processing is shown in Fig. 4.

Area porosity of each planar image was the pore area fraction of that image, which was the average value of all the six planar images corresponding to the same mix proportion. Several methods for characterizing the pore size of porous material have been studied (Sumanasooriya and Neithalath 2009). In this study, average pore size

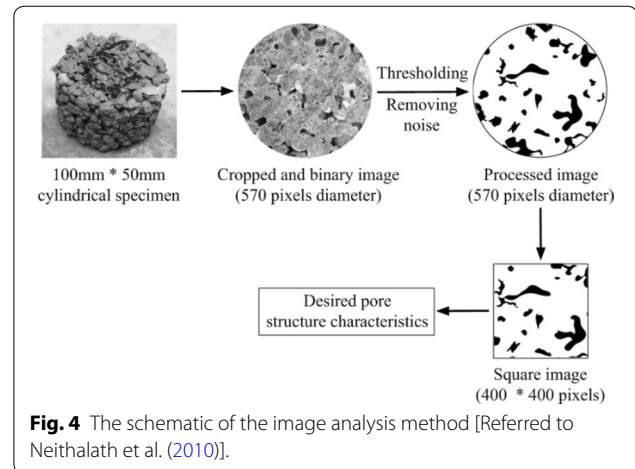


**Fig. 4** The schematic of the image analysis method [Referred to Neithalath et al. (2010)].

**Table 6** Average pore sizes of different mix proportions.

Specimens	Number of images	Average pore size, d (mm)
P1	6	4.07
P2	6	4.48
P3	6	4.59
P4	6	5.22
P5	6	5.81
PS1	6	6.24
PS2	6	5.30
PS3	6	4.79
PSF1	6	4.02

of pervious concrete was calculated by software Image J. Firstly, the area of each individual pore and the number of pores were obtained from each processed binary image, then the equivalent pore size of that image was calculated by considering the pores as circles. The average value of the pore sizes of all the six planar images of same mix proportion was chosen as the representative pore size for that mix proportion.

### 3 Results and Discussion

Results of the aforementioned tests including the pore sizes, pore distribution, volumetric and area porosity, permeability coefficient, compressive strength and freeze–thaw durability are presented in the following section.

#### 3.1 Pore Size

Average pore sizes of pervious concrete with different mix proportions are listed in Table 6. As can be seen from Table 6, the average pore size increases with increasing in the proportion of 10–15 mm coarse aggregate. The average pore size of 100% 5–10 mm specimens

(P1) is 4.07 mm, the average pore sizes are 4.59 mm and 5.81 mm for 50% 5–10 mm (P3) and 0% 5–10 mm (P5) coarse aggregate mixtures respectively. The pore sizes of the specimens of 50% 5–10 mm and 0% 5–10 mm coarse aggregate are 12.78% and 42.75% larger than those of specimens prepared in 100% 5–10 mm coarse aggregate, respectively. The average pore sizes of the specimens modified with 7% additional fine aggregate are larger than that of the specimens of corresponding coarse aggregate proportions. In comparison to 100% 5–10 mm specimens mixed with fine aggregate (PS3) and 100% 5–10 mm specimens mixed with fine aggregate and basalt fiber (PSF1), the addition of fiber could reduce the average pore size of the specimens.

### 3.2 Pore Distribution

Representative planar images of the specimens which are processed by Image J are shown in Fig. 5. In comparison to Fig. 5a, individual pore size in Fig. 5b–e is larger in the mixture with larger proportion of 10–15 mm coarse aggregate, and pore distributions in those mixtures are less homogeneous. By comparing Fig. 5f–h, it can be found that the variation trend of pore distribution with aggregate gradation is similar to the above trend. Figure 5 shows that there is a greater distance between pores for the specimens modified with 7% additional fine aggregate than that in the specimens of corresponding coarse aggregate proportions. It is in consequence of larger distance between pores that distance of stress propagation in the mortar before encountering the pores is able to be longer for these specimens incorporated fine aggregate. In addition, basalt fiber in the 100% 5–10 mm specimens

results in a more homogeneous pore distribution as compared to the 100% 5–10 mm specimens modified with fine aggregate as seen in Fig. 5i, h.

Furthermore, in order to quantitatively describe the homogeneity of pore distribution in the plane images, the homogeneity of pore distribution was transformed into homogeneity of pixel coordinates distribution of pore centroids and pixel area distribution of pores in the plane images. The smaller the standard deviation of the histogram of the pixel coordinate distribution of pore centroids, the more uniform the distribution of the pore centroids in each plane image. The uniformity of the area distribution of the pores was also determined in this way. To be clear, the uniformity of pixel coordinate distribution of pore centroids in the images took precedence over the uniformity of pixel area distribution of pores. Therefore, the pixel coordinates of each pore centroid and the pixel area of each pore in the binary images were extracted through a MATLAB code, and standard deviations of the histogram of their distributions were also calculated.

The standard deviations of the histogram of the pixel coordinates distribution of pore centroids and the pixel area distribution of pores in each plane image in the original Fig. 5 are listed in Table 7. Here, Std1, Std2 and Std are the standard deviation of x direction of pixel coordinates of pore centroid, y direction of pixel coordinates of pore centroid and pixel area of pore, respectively.

As shown in Table 7, the standard deviations of the pixel coordinate of pore centroids and the pixel area of pores increase with increasing in the proportion of 10–15 mm coarse aggregate. The value of Std1\*Std2 of

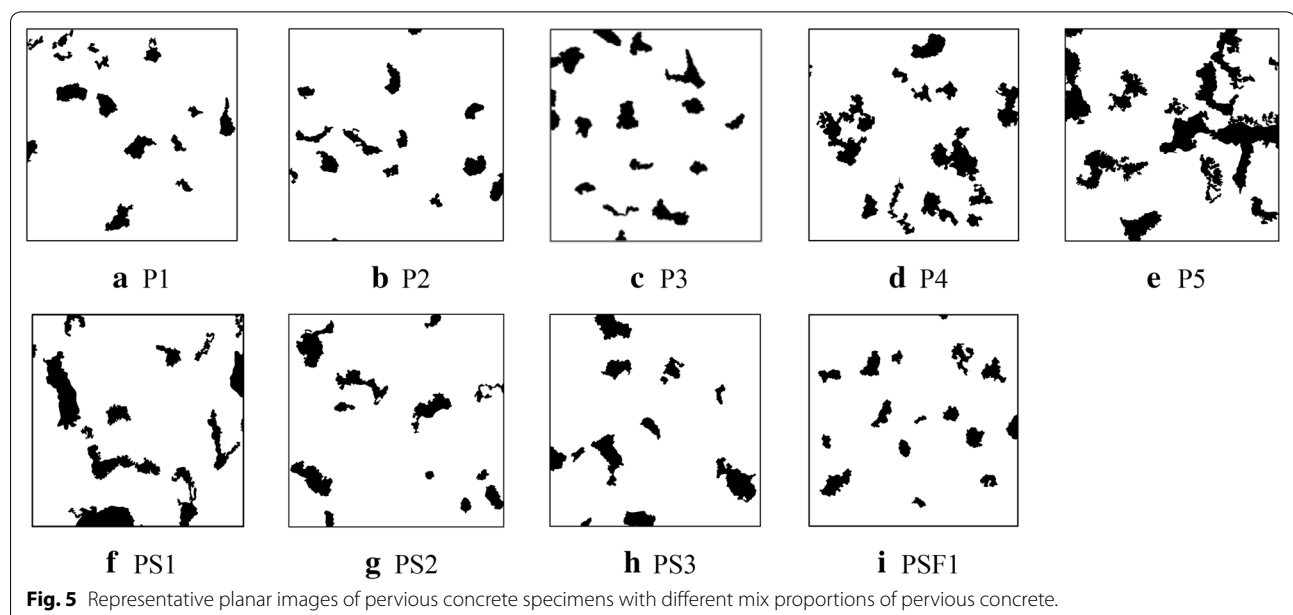
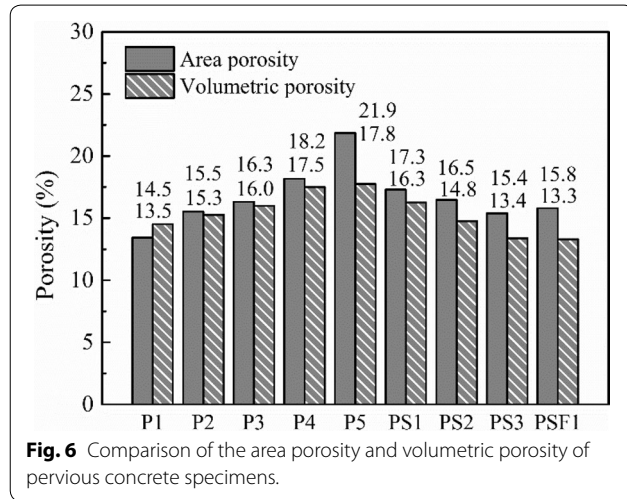


**Fig. 5** Representative planar images of pervious concrete specimens with different mix proportions of pervious concrete.



**Table 7** The standard deviations of the histogram of the pixel coordinates of each pore centroid and the area of each pore of each specimen.

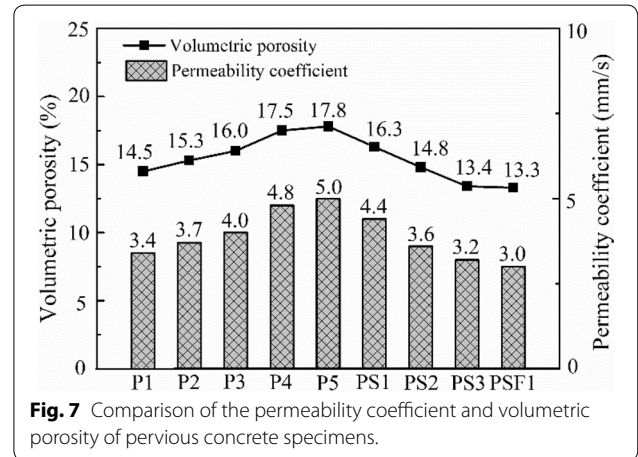
	P1	P2	P3	P4	P5	PS1	PS2	PS3	PSF1
Std1	16.43	11.77	16.81	16.17	14.23	16.83	14.64	13.99	13.55
Std2	13.72	19.19	15.09	15.84	18.18	15.12	15.74	15.30	14.26
Std1*Std2	225.42	225.87	253.66	256.13	258.70	254.47	230.43	214.05	193.22
Std	450.95	485.25	485.31	495.05	598.15	646.45	569.15	509.93	385.95



100% 5–10 mm specimens (P1) is 225.42, the values of Std1\*Std2 are 253.66 and 258.70 for 50% 5–10 mm (P3) and 0% 5–10 mm (P5) coarse aggregate mixtures respectively. The values of Std1\*Std2 of the specimens of 50% 5–10 mm and 0% 5–10 mm coarse aggregate are 12.53% and 14.76% larger than those of specimens prepared in 100% 5–10 mm coarse aggregate, respectively. By comparing the values of Std1\*Std2 of PS1, PS2 and PS3 specimens, similar variation trend of pore distribution with aggregate gradation can be found. From this perspective, the pore distribution of the mixtures with larger proportion of 10–15 mm aggregates are less homogeneous. In addition, the values of Std1\*Std2 are 214.05 and 193.22 for PS3 and PSF1 respectively, therefore, adding basalt fiber to pervious concrete increases the homogeneity of pore distribution in pervious concrete.

### 3.3 Porosity

Figure 6 shows both area porosities obtained from the image analysis method and volumetric porosities of pervious concrete specimens. For no-sand specimens of P1–P5, with an increase in the proportion of 10–15 mm aggregate, there is an increase in the volumetric porosity of the specimens. The average volumetric porosities of 100% 5–10 mm specimens is 14.5%.



The average volumetric porosities are 16.0% and 17.8% for 50% 5–10 mm and 0% 5–10 mm aggregate specimens, respectively. The volumetric porosity of the specimens of 100% 5–10 mm coarse aggregate are 9.38% and 18.54% smaller than those of specimens prepared in 50% 5–10 mm and 0% 5–10 mm coarse aggregate respectively. The volumetric porosities of pervious concrete specimens blended with fine aggregate are found to decrease. In comparison to 100% 5–10 mm aggregate specimens, volumetric porosity of specimens of PS3 modified with 7% additional fine aggregate has a decrease of 7.59%. By comparing PS3 and PSF1, it can be seen that the incorporation of fiber reduces the volumetric porosity slightly. It also can be seen from Fig. 6 that values of area porosities are in reasonable agreement with the volumetric porosities and the variable trends are almost similar.

### 3.4 Permeability Coefficient

Figure 7 shows the permeability coefficients of pervious concrete specimens. The volumetric porosities of the corresponding specimens are also drawn in Fig. 7. It can be seen from no-sand specimens of P1–P5 that with increasing the proportion of 10–15 mm coarse aggregates, the permeability coefficient increases. In comparison to 100% 5–10 mm aggregate specimens, the permeability coefficient of PS3 modified with 7% additional fine

aggregate has a decrease of 5.88%. The permeability coefficients of PS2 and PS1 specimens are 10.0% and 12.0% lower than that of the 50% 5–10 mm aggregate specimens and 0% 5–10 mm aggregate specimens, respectively. The decrease of permeability coefficients of the specimens modified with fine aggregate could partly be attributed to their reduced porosities. The addition of fiber can slightly reduce permeability coefficient of pervious concrete. The permeability coefficient of 100% 5–10 mm specimens modified with both fine aggregate and basalt fiber is 3.0 mm/s, which is smaller than those of 100% 5–10 mm specimens and 100% 5–10 mm specimens modified with fine aggregate.

### 3.5 The Influence of Different Mix Proportion on the Pore Structure Characteristics

Pervious concrete is proportioned using gap-grading coarse aggregates and eliminating sand to create a network of large continuous pores in the material. The permeability coefficient of pervious concrete generally depends on the continuous porosity. The larger the porosity of pervious concrete is, the larger the volume of fluid transport in unit time is, and the larger the permeability coefficient of pervious concrete is.

Coarse aggregate of different particle sizes forms different macro pores between coarse aggregate particles. The larger the particle size of coarse aggregate, the larger the pore between particles. Since the water-to-binder ratio of the specimens in this experiment is the same, the fluidity of cementitious paste is basically the same and the ability of the cementitious paste to fill the pore between particles is also equal. Therefore, with increasing in the proportion of 10–15 mm coarse aggregate, the average pore size, porosity and permeability coefficient of pervious concrete increase.

When adding fine aggregate into pervious concrete, fine aggregate could fill small pores in pervious concrete, increasing the proportion of large pores in pervious concrete. As a result, the average pore size of pervious concrete becomes larger, but the porosity and permeability coefficient of pervious concrete decreases.

In addition to filling some small pores in pervious concrete matrix, the incorporation of fiber also occupies a part of the pore volume between coarse aggregate particles of pervious concrete, so that the average pore size and continuous porosity of the specimen decreases. The decreased porosity of pervious concrete allows less volume of fluid transmission, resulting in the decrease of permeability coefficient.

### 3.6 Compressive Strength

The compressive strengths of specimens are shown in Fig. 8. It can be seen from no-sand specimens of P1–P5

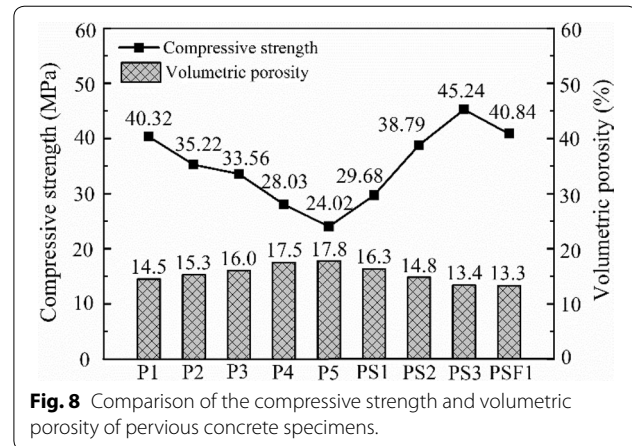


**Fig. 8** Comparison of the compressive strength and volumetric porosity of pervious concrete specimens.

that with increasing the proportion of 10–15 mm aggregate, the compressive strength of specimens decreases. The compressive strength of 100% 5–10 mm specimens is 40.32 MPa, the compressive strengths are 35.22 MPa, 33.56 MPa, 28.03 MPa and 24.02 MPa for 75% 5–10 mm, 50% 5–10 mm, 25% 5–10 mm and 0% 5–10 mm coarse aggregate mixtures respectively. The compressive strength of specimens of 100% 5–10 mm coarse aggregate is 12.65–40.43% higher than those of specimens prepared in different proportion of 10–15 mm aggregate. It may be in consequence of relatively smaller pore size and more homogeneous pore distribution in the mixtures with smaller proportion of 10–15 mm coarse aggregate as described in Sect. 3.2. Lower compressive strength of 0% and 25% 5–10 mm coarse aggregate specimens could partly be attributed to its higher porosities.

Similar trend is seen from specimens modified with fine aggregate (PS1–PS3). The compressive strengths of the specimens blended with fine aggregate are found to increase with decreasing proportion of 10–15 mm coarse aggregate. The compressive strength of PS3 of 100% 5–10 mm aggregate specimens are 15.58% and 23.56% higher than that of the 50% 5–10 mm aggregate specimens and 0% 5–10 mm aggregate specimens, respectively. It can be seen that fine aggregate can improve the compressive strength of pervious concrete, and the most notable improvement is observed in specimens with 0% 5–10 mm aggregate. An argument for increased compressive strengths of the specimens prepared with fine aggregate is larger distance between pores as summarized in Sect. 3.2. As pore spacing increases, the distances of stress propagation in the mortar before encountering neighboring pore is able to be longer, eventually resulting in higher strength.

By comparing PS3 and PSF1, it can be seen that the incorporation of fiber cannot significantly improve in compressive strength. In highly porous structure, fiber is

likely to result in fiber agglomeration and to form stress weak zones, as a result, the improvement of compressive performance of fibers may be offset by the stress weak zones. For very close volumetric porosities, specimens of PS3 and PSF1 are observed to show slight difference in compressive strength. From this point, in addition to porosity, pore structure characteristics can also be assumed to have an important influence on the compressive response of pervious concrete.

### 3.7 Durability

The influences of different proportions of coarse aggregate of two sizes, fine aggregate, fiber and pore structure on freeze–thaw durability of pervious concrete are illustrated in Fig. 9. It can be seen from no-sand specimens of P1–P5 in Fig. 9 that, the general trend shows an increase in the loss rates of compressive strength and loss rates of mass of pervious concrete specimens with an increase in the proportion of 10–15 mm aggregate. The loss rates of compressive strength of 100% 5–10 mm, 50% 5–10 mm and 0% 5–10 mm coarse aggregate specimens at 100 freeze–thaw cycles are 9.28%, 14.11% and 20.55%, respectively. The loss rates of mass of 100% 5–10 mm, 50% 5–10 mm and 0% 5–10 mm coarse aggregate specimens at 100 freeze–thaw cycles are 2.48%, 3.03% and 4.46%, respectively. The reason for the improvement of the freeze–thaw durability of specimens with smaller proportion of 10–15 mm coarse aggregate may be the same as the improvement of compressive strength. As described in Sect. 3.2, pore size in the mixtures with smaller proportion of 10–15 mm coarse aggregate is relatively smaller and pore distribution is more homogeneous, thus resulting in higher freeze–thaw durability for these specimens with smaller proportion of 10–15 mm coarse aggregate.

Incorporation of fine aggregate can reduce the loss rates of compressive strength and mass of pervious concrete specimens. The loss rates of compressive strength of 100% 5–10 mm specimens modified without and with fine aggregate at 50 freeze–thaw cycles are 4.13% and 4.09%, respectively. The loss rate of compressive strength of 50% 5–10 mm specimens modified with fine aggregate at 50 freeze–thaw cycles is 38.34% less than that of specimens prepared without fine aggregates. The loss rate of compressive strength of 0% 5–10 mm specimens modified with fine aggregate at 50 freeze–thaw cycles is 6.37% and has a decrease of 45.93% in comparison to the specimens of P5 without fine aggregate. The results show that the higher the proportion of 10–15 mm aggregate, the more obvious the improvement of freeze–thaw performance of incorporation of fine aggregate. The reduction of loss rate of compressive strength of specimens modified with fine aggregate at 100 freeze–thaw cycles are also observed. Similar trends are found in the loss rates of mass of specimens at 50 freeze–thaw cycles and 100 freeze–thaw cycles. On the one hand, the incorporation of fine aggregate increases the contact points among aggregates and optimizes the interface zone between cement and aggregate. Increased number of contact points and improved pore structure in pervious concrete can improve the bonding force and reduce deterioration rates of pervious concrete specimens. Meanwhile, there is a larger distance between pores of specimens modified with 7% additional fine aggregate than that of specimens of corresponding coarse aggregate proportions as shown in Fig. 5 in Sect. 3.2. It is in consequence of the larger distance between pores that the distance of stress propagation in the mortar before encountering the neighboring pore space is able to be longer, thus resulting in higher freeze–thaw durability for these specimens incorporated of fine aggregate.

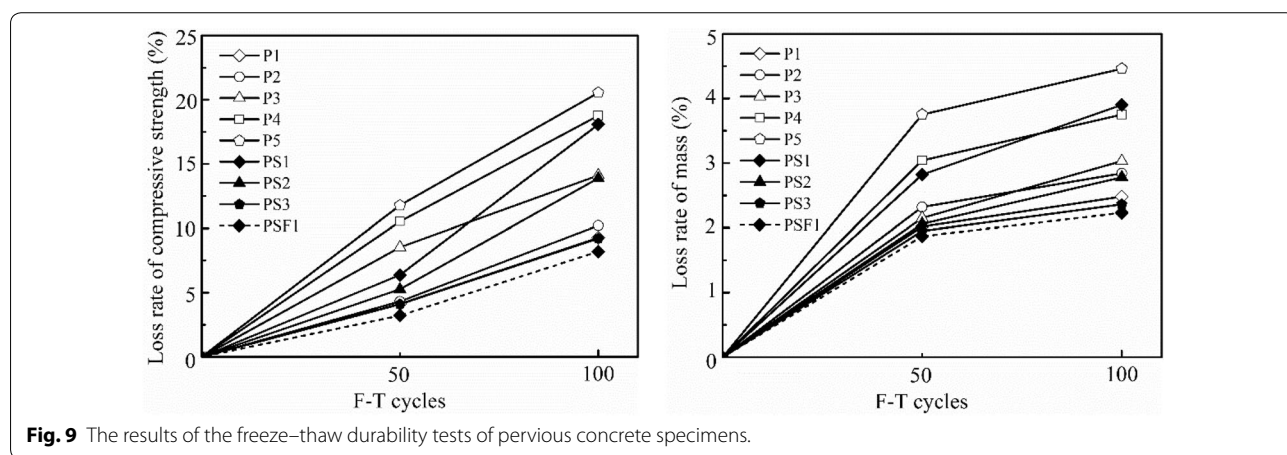


Figure 9 also reveals that incorporation of basalt fiber at a 0.2% volume content can improve the freeze–thaw durability of pervious concrete. The loss rates of compressive strength of 100% 5–10 mm specimens at 50 freeze–thaw cycles is 4.13%, the loss rate of compressive strength of 100% 5–10 mm specimens modified only with fine aggregate at 50 freeze–thaw cycles is 4.09%, and the loss rate of 5–10 mm specimens modified with both fine aggregate and basalt fiber at 50 freeze–thaw cycles is 3.21%. There is a decrease of 22.28% of the loss rate of compressive strength modified with both fine aggregate and basalt fiber at 50 freeze–thaw cycles in comparison with 100% 5–10 mm specimens. The reduction of loss rate of compressive strength of specimens modified with both fine aggregate and basalt fiber at 100 freeze–thaw cycles is also seen in Fig. 9. Similar changes in the loss rate of mass of specimens at 50 freeze–thaw cycles and 100 freeze–thaw cycles are observed in Fig. 9 also. When specimens are cracked due to the repeated freeze–thaw processes, fiber is able to delay the crack initiation. Meanwhile, the bridge connection of fiber can delay the propagation of cracks and reduce loss rates of both compressive strength and mass of pervious concrete. Besides, fiber in the specimens could result in a more homogeneous pore distribution as compared to the specimens without fiber as seen in Fig. 5 in Sect. 3.2, resulting in a better durability for the specimens mixed with basalt fiber.

#### 4 Numerical Validation

In order to verify the correctness of pore structure parameters derived by suggested image analysis method and the validity of suggested reconstruction mechanical model analysis method, three numerical models with different pore structure characteristics are simulated.

##### 4.1 Numerical Model

###### 4.1.1 Size Distribution of Aggregates and Pores

The aggregate proportion in volume of pervious concrete is set as 75%, according to the method introduced in Vipulanandan and Liu (2008). The aggregate size distribution in the Vipulanandan and Liu (2008) is used in this study. Coarse aggregates are generated as irregular convex hexagon. The centroid positions of coarse aggregates in the reconstructed structure models follow the random distribution throughout the entire matrix. The overall area porosity and pore size of the regenerated structure models are in accordance with the actual image analysis results. Pores are generated as regular hexagon. The centroid positions of pores in the reconstructed models also follow the random distribution throughout the entire matrix.

###### 4.1.2 Aggregate and Pore Generation

A generate-and-place procedure is developed to generate the microstructure of pervious concrete in MATLAB. The basic idea is to generate and place aggregates and pores in a repeated manner until the target area is fully packed. The final models are output from CAD software.

###### 4.1.3 Finite Element Mesh Generation and Uniaxial Compression Simulations

Uniaxial compression tests are modeled using ANSYS. The 2D numerical model has a dimension of 150 mm × 150 mm. The microstructure models are meshed using quadrangular solid FE elements (element size is 2 mm).

The solid elements for aggregates and mortar are assumed to have a linear elastic deformation and brittle failure behavior. To obtain the input parameters for numerical simulation, series of laboratory experiments were conducted to determine the actual pervious concrete parameters before the numerical modeling. To obtain Young’s modulus and Poisson’s ratio of concrete matrix and basalt, specimens that can be used in the material elastic modulus tester were prepared. The mix proportion of concrete matrix specimen was the same as that of P3 specimens used in the test. The water-binder ratio was 0.22. Fly ash and silica fume were incorporated by replacing 10% and 7.5% of the cement by weight, respectively. At the same time, the basalt specimens were purchased from the stone field in which the coarse aggregate were bought in the experiment. Upon completion of specimen preparation, a testing institution was entrusted to measure the Young’s modulus and Poisson’s ratio of the materials. In addition, the densities of materials were obtained by measuring the weight per unit volume in the laboratory. Material parameters are listed in Table 8.

The boundary condition of each model is chosen as a roller support at the bottom surface, and is fixed at the middle point of that surface. Displacement-controlled loading scheme was applied to the top surface and the other two sides are kept as free. Maximum strain failure criterion is selected as the failure criteria for the simulations.

**Table 8** Material parameters.

	Density $\rho$ ( $10^{-9}$ tone/ mm <sup>3</sup> )	Young’s modulus E (MPa)	Poisson’s ratio $\nu$
Aggregate	2.5	70,000	0.2
Mortar	2.2	25,000	0.2

## 4.2 Numerical Results

### 4.2.1 Comparison of the Stress–Strain Plots of the Simulation and Experimental Results

The stress–strain curves of pervious concrete specimens obtained from the numerical tests are plotted in Fig. 10 and are compared with the laboratory stress–strain plots. It can be seen that experimental and numerical stress–strain plots show close proximity, even though failure pattern of the numerical model is not consistent exactly with that of the experimental results. In initial stage of the pre-peak, the slope of numerical simulation results is greater and numerical results show a stiffer response, mainly because the chance of microstructure that can be condensed and reorganized are ignored. After that, the experimental plot and the simulated plot tend to be the same (with the deviation of the Young’s Modulus of approximately 0.6%) and reach almost the same peak value (with deviation of approximately 7%).

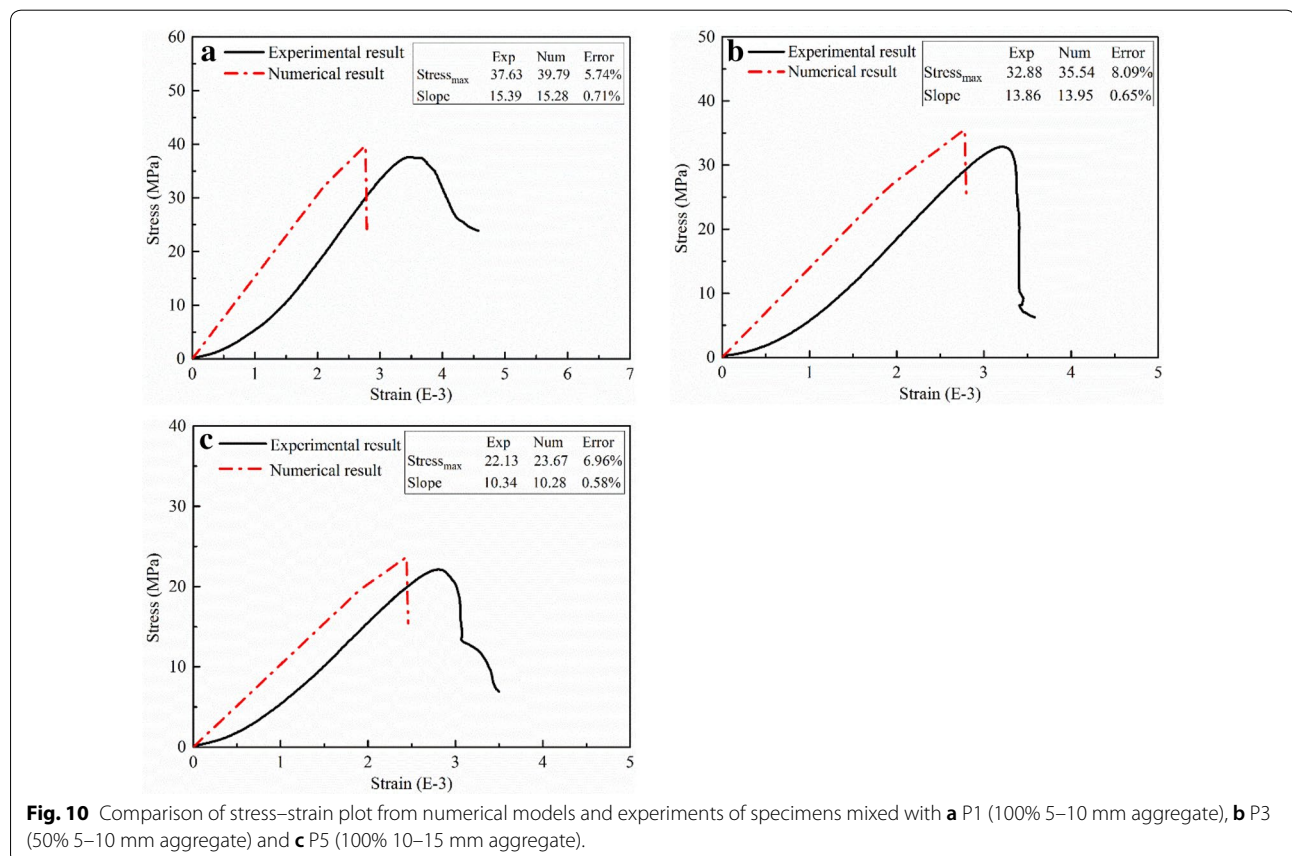
### 4.2.2 Comparison of the Failure and Cracks of the Simulation and Experimental Results

Figure 11 shows a comparison of failure patterns in pervious concrete matrix revealed by experimental specimens and numerical models. The failure appears

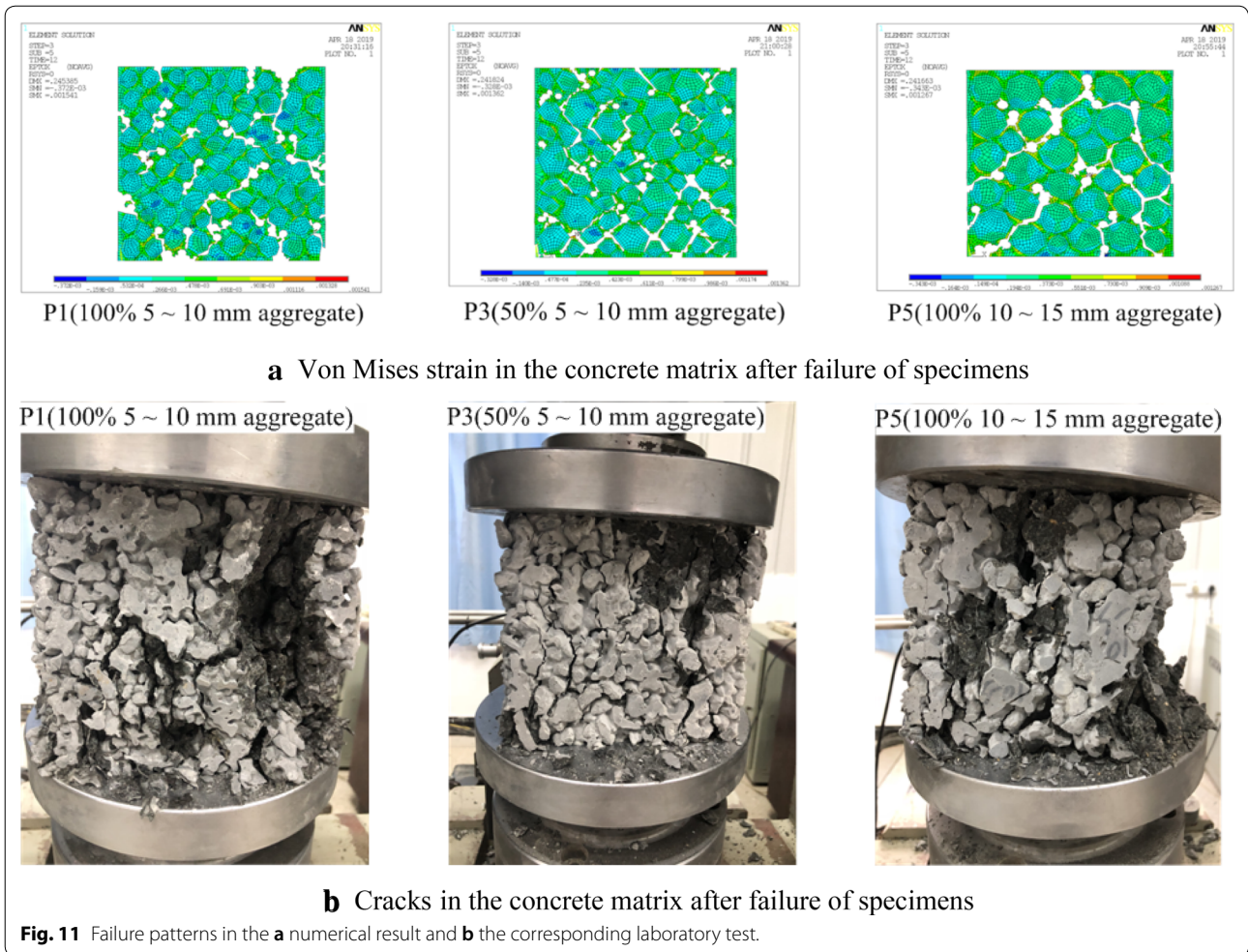
firstly in the weak matrix zone induced by randomly distributed pores and interfaces between aggregate and cementing paste. Subsequently, the process gradually propagates and finally forms integrated cracks. The integrated cracks are mainly distributed at the interfaces between aggregate and cementing paste. It can be observed that the cracks and failure initiated by the applied displacement in the numerical models (Fig. 11a) are generally in close agreement with that obtained from the experimental tests (Fig. 11b).

## 5 Conclusion

A total of 9 pervious concrete specimens with different pore structures were prepared by using combinations of two different aggregate sizes. Compressive strength, porosity, permeability and freeze–thaw durability of pervious concrete were tested by lab experiments. Pore structure characteristics of pervious concrete based on image analysis were extracted and analyzed, and the regenerated numerical models through a MATLAB code were meshed and solved in ANSYS. Based on these work, the following conclusions can be drawn:



**Fig. 10** Comparison of stress–strain plot from numerical models and experiments of specimens mixed with **a** P1 (100% 5–10 mm aggregate), **b** P3 (50% 5–10 mm aggregate) and **c** P5 (100% 10–15 mm aggregate).



- (1) The average pore size of pervious concrete increases with increasing in the proportion of coarse aggregate with size of 10–15 mm. The addition of 7% fine aggregate increases average pore size of pervious concrete, while the addition of fiber reduces average pore size of pervious concrete.
- (2) The pore distribution in the mixtures with larger proportion of 10–15 mm coarse aggregate is less homogeneous. However, fiber results in a more homogeneous pore distribution of pervious concrete. The distance between pores for pervious concrete modified with 7% additional fine aggregate is larger than that of corresponding coarse aggregate proportions.
- (3) The compressive strength of no-sand pervious concrete decreases with an increase in the proportion of the 10–15 mm aggregate. The fine aggregate can improve compressive strength of pervious concrete. However, the incorporation of fiber does not provide significant improvement in compressive strength.
- (4) The volumetric porosities and area porosities of no-sand pervious concrete increase with an increase in proportion of 10–15 mm aggregate. The volumetric porosities of pervious concrete specimens blended with fine aggregate are found to decrease. The general trends of volumetric porosities and permeability coefficients are similar with the mix proportion of this experiment.
- (5) The loss rates of compressive strength and of mass of no-sand pervious concrete increase with an increase in proportion of 10–15 mm aggregate. Incorporation of fine aggregate and basalt fiber at a 0.2% volume content can both improve the freeze–thaw durability of pervious concrete.
- (6) The simulated stress–strain plots and cracks initiated by displacement loading mode from the micro-structure numerical models are in close match with

that from the lab experiments, which confirms the correctness of proposed pore structural parameters derived by image analysis.

#### Acknowledgements

Not applicable.

#### Authors' contributions

RL carried out the experiment and numerical simulation studies. YC and QJ participated in the numerical simulation studies. XM, KW and SL participated in the experiment studies. SC participated in the revision of the paper. All authors read and approved the final manuscript.

#### Authors' information

RL, PhD Candidate in School of Civil Engineering, Wuhan University, Wuhan, Hubei, 430072, P.R. China, E-mail: 18202752427@163.com. YC, Professor in School of Civil Engineering, Wuhan University, Wuhan, Hubei, 430072, P.R. China, E-mail: yinchi@whu.edu.cn. SC, Senior Engineer in Institute of Defense Engineering, AMS, PLA, Beijing, 100850, P.R. China, E-mail: chenshengyun-jia@163.com. QJ, Professor in School of Civil Engineering, Wuhan University, Wuhan, Hubei, 430072, P.R. China, E-mail: jqh1972@whu.edu.cn. XM, PhD Candidate in School of Civil Engineering, Wuhan University, Wuhan, Hubei, 430072, P.R. China, E-mail: xymeng1994@163.com. KW, Master's Student in School of Civil Engineering, Wuhan University, Wuhan, Hubei, 430072, P.R. China, E-mail: 13163332433@163.com. SL, Master's Student in School of Civil Engineering, Wuhan University, Wuhan, Hubei, 430072, P.R. China, E-mail: 2201963122@qq.com.

#### Funding

The work reported in this paper has received financial supports from the National Key R&D Program of China (No. 2018YFC1505005). These supports are gratefully acknowledged.

#### Availability of data and materials

Not applicable.

#### Ethics approval and consent to participate

Not applicable.

#### Competing interests

The authors declare that they have no conflict of interest.

#### Author details

<sup>1</sup> School of Civil Engineering, Wuhan University, Wuhan 430072, Hubei, People's Republic of China. <sup>2</sup> Institute of Defense Engineering, AMS, PLA, Beijing 100850, People's Republic of China.

Received: 15 July 2019 Accepted: 23 March 2020

Published online: 11 June 2020

#### References

- ACI 522R-10. (2010). *Report on pervious concrete*. Farmington Hills: American Concrete Institute.
- Akand, L., Yang, M. J., & Gao, Z. L. (2016). Characterization of pervious concrete through image based micromechanical modeling. *Construction and Building Materials*, 114(1), 547–555.
- ASTM C1754/C1754-12. (2012). *Standard test method for density and void content of hardened pervious concrete*. West Conshohocken: ASTM International.
- ASTM C666/C666M-15. (2015). *Standard test method for resistance of concrete to rapid freezing and thawing*. West Conshohocken: ASTM International.
- ASTM D5856-15. (2015). *Standard test method for measurement of hydraulic conductivity of porous material using a rigid-wall, compaction-mold permeameter*. West Conshohocken: ASTM International.
- Bonicelli, A., Giustozzi, F., & Crispino, M. (2015). Experimental study on the effects of fine sand addition on differentially compacted pervious concrete. *Construction and Building Materials*, 91(30), 102–110.
- Carsana, M., Tittarelli, F., & Bertolini, L. (2013). Use of no-fines concrete as a building material: Strength, durability properties and corrosion protection of embedded steel. *Cement and Concrete Research*, 48, 64–73.
- Chandruppa, A. K., & Biligiri, K. P. (2016). Influence of mix parameters on pore properties and modulus of pervious concrete: an application of ultrasonic pulse velocity. *Materials and Structures*, 49(12), 5255–5271.
- Chen, Y., Wang, K. J., Wang, X. H., & Zhou, W. F. (2013). Strength, fracture and fatigue of pervious concrete. *Construction and Building Materials*, 42, 97–104.
- Chindaprasit, P., Hatanaka, S., Mishima, N., Yuasa, Y., & Chareerat, T. (2009). Effects of binder strength and aggregate size on the compressive strength and void ratio of porous concrete. *Int J Min Met Mater*, 16(6), 714–719.
- Čosić, K., Korat, L., Ducman, V., & Netinger, I. (2015). Influence of aggregate type and size on properties of pervious concrete. *Construction and Building Materials*, 78(1), 69–76.
- Deo, O., & Neithalath, N. (2010). Compressive behavior of pervious concretes and a quantification of the influence of random pore structure features. *Materials Science and Engineering: A*, 528(1), 402–412.
- Deo, O., & Neithalath, N. (2011). Compressive response of pervious concretes proportioned for desired porosities. *Construction and Building Materials*, 25(11), 4181–4189.
- EN 197-1:2011. (2011). *Cement-Part 1: Composition, specifications and conformity criteria for common cements*. Dublin: National Standards Authority of Ireland.
- GB 175-2007. (2007). *Common portland cement*. China: China Standards Press.
- GB/T 50082-2009. (2009). *Standard for test methods of long-term performance and durability of ordinary concrete*. China: China Building Industry Press.
- Haselbach, L. M., Valavala, S., & Montes, F. (2006). Permeability predictions for sand clogged Portland cement pervious concrete pavement systems. *Journal of Environmental Management*, 81(1), 42–49.
- Hesami, S., Ahmadi, S., & Nematzadeh, M. (2014). Effects of rice husk ash and fiber on mechanical properties of pervious concrete pavement. *Construction and Building Materials*, 53(28), 680–691.
- Huang, B. S., Wu, H., Shu, X., & Burdette, E. G. (2010). Laboratory evaluation of permeability and strength of polymer-modified pervious concrete. *Construction and Building Materials*, 24(5), 818–823.
- Ibrahim, A., Mahmoud, E., Yamin, M., & Patibandla, V. C. (2014). Experimental study on Portland cement pervious concrete mechanical and hydrological properties. *Construction and Building Materials*, 50(15), 524–529.
- Jimma, B. E., & Rangaraju, P. R. (2014). Film-forming ability of flowable cement pastes and its application in mixture proportioning of pervious concrete. *Construction and Building Materials*, 71(30), 273–282.
- Joshaghani, A., Ramezani-pour, A. A., & Jaberizadeh, M. (2014). Mechanical characteristic of pervious concrete considering the gradation and size of coarse aggregates. *Res J Environ Earth Sci*, 6(9), 437–442.
- Kevern, J. T., Biddle, D., & Cao, Q. (2015). Effects of macrosynthetic fibers on pervious concrete properties. *Journal of Materials in Civil Engineering*, 27(9), 06014031.
- Kevern, J. T., Wang, K. J., & Schaefer, V. R. (2010). Effect of coarse aggregate on the freeze-thaw durability of pervious concrete. *Journal of Materials in Civil Engineering*, 22(5), 469–475.
- Luck, J. D., Workman, S. R., Coyne, M. S., & Higgins, S. F. (2008). Solid material retention and nutrient reduction properties of pervious concrete mixtures. *Biosystems Engineering*, 100(3), 401–408.
- Mrakovčić, S., Čeh, N., & Jugovac, V. (2014). Effect of aggregate grading on pervious concrete properties. *Gradevinar*, 66(2), 107–113.
- Neithalath, N. (2007). Extracting the performance predictors of enhanced porosity concretes from electrical conductivity spectra. *Cement and Concrete Research*, 37(5), 796–804.
- Neithalath, N., Sumanasooriya, M. S., & Deo, O. (2010). Characterizing pore volume, sizes, and connectivity in pervious concretes for permeability prediction. *Materials Characterization*, 61(8), 802–813.
- Nguyen, D. H., Sebaibi, N., Boutouil, M., Leleyter, L., & Baraud, L. (2014). A modified method for the design of pervious concrete mix. *Construction and Building Materials*, 73(30), 271–282.

- Rangelov, M., Nassiri, S., Haselbach, L., & Englund, K. (2016). Using carbon fiber composites for reinforcing pervious concrete. *Construction and Building Materials*, 126(15), 875–885.
- Shen, S. H., Burton, M., Jobson, B., & Haselbach, L. (2012). Pervious concrete with titanium dioxide as a photocatalyst compound for a greener urban road environment. *Construction and Building Materials*, 35, 874–883.
- Sumanasooriya, M. S., & Neithalath, N. (2009). Stereology-and morphology-based pore structure descriptors of enhanced porosity (pervious) concretes. *ACI Materials Journal*, 106(5), 429–438.
- Tittarelli, F., Carsana, M., & Bellezze, T. (2013). Corrosion behavior of reinforced no-fines concrete. *Corrosion Science*, 70, 119–126.
- Tittarelli, F., Carsana, M., & Ruello, M. L. (2014). Effect of hydrophobic admixture and recycled aggregate on physical-mechanical properties and durability aspects of no-fines concrete. *Construction and Building Materials*, 66(15), 30–37.
- Vipulanandan, C., & Liu, J. (2008). Glass-fiber mat reinforced epoxy coating for concrete in sulfuric acid environment. *Cement and Concrete Research*, 32(2), 205–210.
- Wong, H. S., Head, M. K., & Buenfeld, N. R. (2006). Pore segmentation of cement-based materials from back scattered electron images. *Cement and Concrete Research*, 36(6), 1083–1090.
- Wu, H., Liu, Z., Sun, B. B., & Yin, J. (2016). Experimental investigation on freeze-thaw durability of Portland cement pervious concrete (PCPC). *Construction and Building Materials*, 117(1), 63–71.
- Wu, H. J., Zhao, J., & Wang, Z. C. (2013). Study on micro-structure and durability of fiber concrete. *Res J Appl Sci Eng Technol*, 5(2), 659–664.
- Xu, G. L., Shen, W. G., Huo, X. J., Yang, Z. F., Wang, J., Zhang, W. S., et al. (2018). Investigation on the properties of porous concrete as road base material. *Construction and Building Materials*, 158(15), 141–148.
- Yang, J., & Jiang, G. L. (2003). Experimental study on properties of pervious concrete pavement materials. *Cement and Concrete Research*, 33(3), 381–386.
- Yang, Z. F., Ma, W., Shen, W. G., & Zhou, M. K. (2008). The aggregate gradation for the porous concrete pervious road base material. *J Wuhan Univ Technol*, 23(3), 391–394.
- Zhong, R., & Wille, K. (2015). Material design and characterization of high performance pervious concrete. *Construction and Building Materials*, 98(15), 51–60.

### Publisher's Note

Springer Nature remains neutral with regard to jurisdictional claims in published maps and institutional affiliations.

Submit your manuscript to a SpringerOpen<sup>®</sup> journal and benefit from:

- Convenient online submission
- Rigorous peer review
- Open access: articles freely available online
- High visibility within the field
- Retaining the copyright to your article

---

Submit your next manuscript at ► [springeropen.com](https://www.springeropen.com)

---